# The structural amphiphilicity of cellulose nanocrystals characterized from their cohesion parameters

Charles Bruel[1], Jason R. Tavares, Pierre J. Carreau, Marie-Claude Heuzey[2]

Research Center for High Performance Polymer and Composite Systems (CREPEC), Chemical Engineering Department, Polytechnique Montreal, P.O. Box 6079, Stn Centre-Ville, Montreal, QC H3C 3A7, Canada.

**Abstract**

Cellulose nanocrystals (CNCs), usually considered as isotropically polar nanoparticles, are sheet-like crystalline assemblies of cellulose chains. Here, we link the anisotropy of the CNC structure to an amphiphilic behavior in suspension. The Hansen solubility parameters (HSP: $\delta_D; \delta_P; \delta_H$) of wood-based $H_2SO_4$-hydrolyzed CNCs were measured from sedimentation tests in a wide set of 59 solvents and binary mixtures. Two sets of cohesion parameters corresponding to a polar surface (18.1; 20.4; 15.3) (0.5; 0.5; 0.4) $MPa^{1/2}$ and to a mildly non-polar one (17.4; 4.8; 6.5) (0.3; 0.5; 0.6) $MPa^{1/2}$ were determined, with respective solubility radii of 7.8 and 2.1 $MPa^{1/2}$. The polar sphere is thought to correspond to the (110)&$(1\bar{1}0)$ surfaces of cellulose $I_\beta$ nanocrystals, while the smaller non-polar sphere is coherent with the exposure of (200) surfaces. The HSP graph provides new insights on the amphiphilic nature of CNCs and a mapping of their chemical affinity for solvents and polymer matrices.

*Keywords:*
cellulose nanocrystals, surface properties, structure-property relationships, chemical affinity, amphiphilicity, Hansen solubility parameters

[1]charles.bruel@polymtl.ca
[2]marie-claude.heuzey@polymtl.ca

## 1. Introduction

D-glucopyranose polymerization produces, through a dehydration, polysaccharides such as starch, glycogen, dextran, and cellulose (Dufresne, 2017; French, 2017). In (1,4)-linked macromolecules, anhydroglucose rings are locked in a chair conformation where all their hydrophilic hydroxyl groups are in equatorial position while all their more hydrophobic C-H bonds are axial. For α-(1,4)-linked polysaccharides, such as dextrins, it results in an apolar behavior in solution (Dufresne, 2017), a feature famously exploited in cyclodextrins whose structure forms a cavity rich in C-H bonds that may be used to encapsulate hydrophobic chemicals (Marques, 2010), including for delivery in living organisms (Chaturvedi et al., 2011).

Although being insoluble in water, amorphous cellulose, a β-(1,4)-linked polymer of anhydroglucopyranose (Fig. 1.a&b), does not display such a marked apolarity in solution (Medronho et al., 2012; Dufresne, 2017). Its structural anisotropy, and its resulting amphiphilicity (Medronho et al., 2012), are however re ected in the crystalline networks cellulose chains form in living organisms such as plants, fungi, algae, bacteria, or tunicates (Moon et al., 2011; Hamad, 2017). From the various allomorphs (Moon et al., 2011; Dufresne, 2017), cellulose $I_\alpha$ (Nishiyama et al., 2003) and $I_\beta$ (Nishiyama et al., 2002) are the only ones that may be found naturally in land plants (Moon et al., 2011). They both reproduce on the nanocrystal level the anisotropy of their monomeric unit. Indeed, cellulose chains assemble in sheets, parallel to the equatorial planes of the anhydroglucose rings, which then stack up to form multilayer crystalline structures, crystallites (Fig. 1.c) (Jarvis, 2003; Li & Renneckar, 2011). Intra and intersheet cohesions are respectively insured by interchain OH-O hydrogen bonds and by weaker interchain CH-O and van der Waals interactions (Jarvis, 2003; Nishiyama, 2017). The formation of these van der Waals interactions is thought to be the initial step through which cellulose chains crystallize (Cousins & Brown, 1995).

Hydrolysing cellulosic feedstocks in acidic conditions, usually with sulfuric acid, digests their amorphous and non-cellulosic contents while mostly preserving their crystalline parts (Dufresne, 2017; Moon et al., 2011; Hamad, 2017). Under harsh enough conditions, the treatment yields highly crystalline cellulose-made particles, cellulose nanocrystals (CNCs). They are hypothesized to be made of several adjacent crystallites (Uhlig et al., 2016; Ding et al., 2012, 2014) assembled with a right-handed chirality (Usov et al., 2015). Introduction of sulfate half-ester groups at CNC surface during the

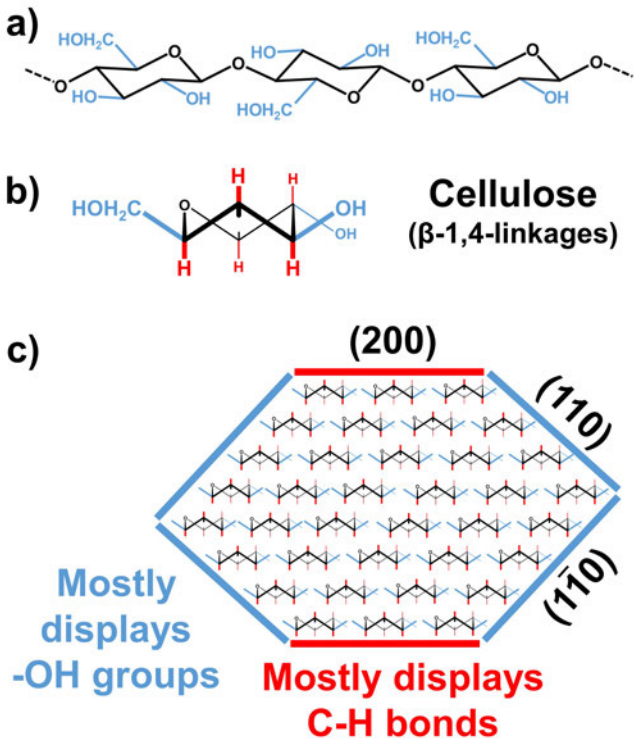


Figure 1: Anisotropy of cellulose. (a) Cellulose, aβ-(1,4)-linked polymer of anhydroglucopyranose (French, 2017), has its monomeric units locked in a conformation where all their hydroxyl substituents (in blue) are in equatorial position while their C-H bonds (in red) are axial as exempli ed in a pro le view (b) . (c) The structure of cellulose I crystallite re ects this anisotropy as cellulose chains are arranged in sheets held together by OH-O hydrogen bonds, which then stack-up through the formation of CH-O H-bonds and van der Waals interactions (Jarvis, 2003; Li & Renneckar, 2011). Based on Ding and Himmel's model (Ding & Himmel, 2006), the resulting crystallite displays up to three kind of surfaces corresponding to the lattice planes (110), (1$\bar{1}$0), and (200) of its crystalline unit. The latter displays mostly C-H bonds, while the two former are rich in hydroxyl groups.

hydrolysis provides them with an electrostatic stabilization upon suspension in water and with interesting self-organization properties (Liu et al., 2011; Hamad, 2017).

CNCs, especially sulfated ones, are usually described as polar particles, which stems from the difficulty encountered to disperse them in non-polar solvents and polymer matrices (Hamad, 2017). Although arising from experimental observations, this description is at odd with the amphiphilic behavior that can be expected from CNC anisotropic structure. Analysis of wide

(WAXS) and small angle X-ray scattering (SAXS) (Elazzouzi-Hafraoui et al., 2008; Sèbe et al., 2012) as well as high resolution atomic force microscopy (AFM) (Ding et al., 2006; 2012; 2014) indeed suggests that up to three kinds of lateral surfaces are displayed by the nanocrystals extracted from cellulose $I_\beta$ sources (Fig. 1.c), by far the most common allomorph in higher plants –wood included (Atalla & Vanderhart, 1999; Habibi et al., 2010). Within the crystalline unit, they correspond respectively to the lattice planes (110), $(1\bar{1}0)$, and (200) (Ding & Himmel, 2006; Brown, 1996). The latter, parallel to the sheets plane, displays mostly C-H bonds, while the two former intersect the plane of the sheets and thus display hydroxyl groups (Fig. 1.c). Molecular dynamic simulations suggests that (110) and $(1\bar{1}0)$ surfaces have similar hydrophilicity (Heiner et al., 1998; Matthews et al., 2006) and surface energies (Yamane et al., 2006), while (200) surfaces are expected to be more hydrophobic, with higher water contact angle (Mazeau & Rivet, 2008) and lower surface energies (Yamane et al., 2006) (Table 1).

Table 1: Cellulose nanocrystal surface properties according to the lattice plane displayed. $\delta_T$ is the total solubility parameter. $\delta_D$, $\delta_P$, and $\delta_H$ are its decomposition in term of dispersive, polar, and hydrogen bonding components, respectively (Hansen, 2007). $R_0$ is the HSP radius.

| Lattice plane | | (110) | $(1\bar{1}0)$ | (200) |
|---|---|---|---|---|
| Surface energy[a] | $mN\,m^{=1}$ | 155 | 155 | 92 |
| Water contact angle[b] | ° | 43 | - | 95 |
| $\delta_T$ | $MPa^{1/2}$ | 31.3 1.4 | | 19.2 2.7 |
| $\delta_D$ | $MPa^{1/2}$ | 18.1 0.5 | | 17.4 0.3 |
| $\delta_P$ | $MPa^{1/2}$ | 20.4 0.5 | | 4.8 0.5 |
| $\delta_H$ | $MPa^{1/2}$ | 15.3 0.4 | | 6.5 0.6 |
| $R_0$ | $MPa^{1/2}$ | 7.8 | | 2.1 |

[a] Modeled values as calculated by Yamane et al. (2006).
[b] Modeled values as calculated by Mazeau & Rivet (2008).

Chemically, a proof that CNCs display hydroxyl groups rich surfaces –which would correspond to the (110) and $(1\bar{1}0)$ lattice planes– may be provided easily by attempting to functionalize them (Eyley & Thielemans, 2014). $(1\bar{1}0)$ lattice planes have furthermore already been observed by atomic force microscopy on cellulose $I_\beta$ samples (Kuutti et al., 1995). The detection of unreactive C-H bonds rich surfaces –which would correspond to the (200) lattice plane– is, however, harder to achieve. The main clue is that the display of (200) lattice planes by CNCs should result in a certain level of amphiphilic-

ity, as experimentally confirmed : stable suspensions of CNCs in chloroform have been reported (Yu & Qin, 2012; Yu et al., 2012). This mildly non-polar solvent may also form inclusions in cellulose I fibers (Wade & Creely, 1974). It is worth noting that not every work reports a good dispersion in chloroform (Yoo & Youngblood, 2016; Petersson et al., 2007) and it remains to be seen whether this divergence has to be attributed to differences in feedstock, hydrolysis conditions, or protocol of dispersion, such as the intensity of the ultrasonication for instance. Other hydrophobic interactions of cellulose include those with cellulases (Himmel et al., 2007; Mazeau & Rivet, 2008) and congo red (Mazeau & Wyszomirski, 2012; Conley et al., 2017b,a) whose aromatic parts are both thought to adsorb primarily on the (200) surfaces.

Although these preliminary results point toward a chemical influence of (200) surfaces for some CNC suspensions, thus conforming WAXS, SAXS, and AFM observations, none of them really isolate their potential contribution from the stronger influence of the (110) and $(1\bar{1}0)$ surfaces.

In this work, we apply a thermodynamic approach based on the Hansen solubility parameters (HSP) and on sedimentation tests using 59 solvents and binary mixtures, to isolate experimentally the influence of the hydrophobic (200) surfaces from the predominant one of the more hydrophilic (110) and $(1\bar{1}0)$ surfaces (as reported in Table 1). These investigations result into a mapping of CNC affinity for common solvents and polymers. The identification of an amphiphilic behavior for the nanocrystals establishes a direct link between their structure and their surface properties.

## 2. Materials and methods

### *2.1. Materials*

CNCs, provided by Celluforce (Montreal, QC, Canada) as a spray-dried powder, were obtained from Kraft wood pulp by a sulfuric acid hydrolysis treatment followed by a neutralization with sodium hydroxide (NaOH). Previous work from our team on CNCs from the same batch demonstrated that these particles are in average  165 nm long and  13 nm wide with a sulfur content equivalent of 3.4 sulfate half ester (O  $SO_3H$) per 100 anhydroglucose units (Beuguel et al., 2018b). The X-ray diffractogram is typical of $I_\beta$ cellulose (Elazzouzi-Hafraoui et al., 2008; Sèbe et al., 2012) and the crystallinity index was found to be of 81 %.

To obtain the dimensions of the CNCs the following procedure was applied (Beuguel et al., 2018b). A drop of a sonicated water suspension of

CNCs, diluted at 10 $\mu g_{CNCs}$ $mL^{-1}_{water}$, was deposited on a copper TEM grid covered by a 5 to 6 nm-thick layer of pure carbon. Average dimensions, with standard deviations in the range of 10 %, were obtained from measurements of over 100 particles performed on transmission electronic microscopy (TEM) micrographs obtained at 200 kV with a bright eld imaging Jeol JEM 2100F (Beuguel et al., 2018b). The sulfur content was measured from X-Ray energy dispersive spectroscopy (EDX) analysis performed on the CNC spray-dried powder with a Tabletop Hitachi TM3030+ scanning electron microscope. Scanning of three samples on di erent locations, for a total of ten scans, yielded a sulfur over carbon (S/C) atomic ratio of 0.0057 with a standard deviation of 0.0005 (Beuguel et al., 2018b). The oxygen over carbon (O/C) atomic ratio was of 0.79 0.02, very close to the theoretical value of 0.83 for cellulose, and is indicative of a high level of purity for the nanocrystals (Siqueira et al., 2010). The CNC crystallinity was measured through X-ray di raction (XRD) with a X'pert instrument (Philips) operating with Cu K α radiations (wavelength of 0.1542 nm generated at 50 kV with a current of 40 mA. Scan type was continuous with an angle $\theta$2 varying from 5.01° to 49.99° with steps of 0.02° and a scan time of 1 s per step. The crystallinity index, IC, was measured as $IC = 1 - I_{AM} / I_{200}$, according to Segal's empirical method (Segal et al., 1959). $I_{AM}$ and $I_{200}$ are the intensities of the amorphous peak ($2\theta = 18.85°$) and of the peak corresponding to the (200) lattice planes ($2\theta = 23.01°$), respectively.

Organic solvents employed were purchased from commercial suppliers at high purity grade (purity >99 %, see Table A.1). The only exceptions are ethanol, used in its denatured form (purity of 95 %), and d-limonene (purity of 96 %), as higher purity grades of d-limonene are generally not available commercially. Distilled water was employed. Binary mixtures were prepared by mixing pure solvents. Densities and viscosities of solvents and mixtures at 25 °C were obtained by averaging experimental values reported in the specialized literature (Tables A.1&A.2).

### *2.2. Sedimentation tests*

#### *2.2.1. Protocol*

10 mL of the di erent solvents and binary mixtures were added to 0.1 g of CNCs in a glass vials of radius 2.1 cm. An ultrasonic probe (Cole-Parmer) operating at a frequency of 20 kHz with a CV334 converter and a tapered microtip was used to disperse the CNCs. The treatment had a power of 25 W and was applied with a pulse cycle ON OFF of 5 s 2 s for a total

energy of 10,000 J $g^{-1}_{CNCs}$. Previous experimentation demonstrated that such a treatment do not result into desulfation of the CNCs (Beuguel et al., 2018b). The vials were placed in an ice bath to avoid any overheating during the ultrasonication. CNC suspensions (10 $mg_{CNCs}$ $mL^{-1}_{solvent}$) were then allowed to rest at 25 °C for a relative sedimentation time, RST = 1.18 $10^{11}$ $s^2m^{-2}$. Calculated with Eq. 1 (Hansen, 2007), it corresponds for instance to an absolute sedimentation time, $t_{sed}$, of 12.1 h in acetone, 48.0 h in water, or 1140 h in ethylene glycol (Tables A.1&A.2). Once the time of sedimentation had elapsed, three kinds of qualitative behaviors were observed for CNC sedimentation. Graded on a scale from best, 2, to worst, 0, they correspond respectively to: 2- a suspension without formation of any sediment (as shown in Fig. 2.a for DMSO), 1- a turbid suspension in which a sediment is formed (dichloromethane), and 0- all remaining cases in which a sediment is formed and the suspension is clear enough for text to be read through (toluene). The only exception to the aforementioned protocol is the sedimentation in triethanolamine, which was interrupted after a RST of 1.18 $10^{10}$ $s^2m^{-2}$ (10% of the standard RST). Due to the very high viscosity of triethanolamine, it corresponds to a time of sedimentation $t_{sed}$ of 4100 h. Its behavior is clearly that of a 0-grade solvent (Fig. A.1).

$$t_{sed} = RST \frac{\eta_{solv}}{\rho_{CNCs} \quad \rho_{solv}} \tag{1}$$

*2.2.2.* RST *calibration*

Sulfating CNCs provides them with surface charges, generating electrostatic stabilization. It is a kinetic effect: the thermodynamically favored outcome of a colloidal suspension is the coagulation of the particles (Kronberg et al., 2014). For electrostatic stabilization to manifest, there has to be dissociation between the negatively charged CNCs and their counter-ions, an outcome favored in solvents whose dielectric constants, $\varepsilon_{solv}$, are high (Kronberg et al., 2014). HSP characterization is a thermodynamic approach and a RST of 1.18 $10^{11}$ $s^2m^{-2}$ was selected following a calibration aimed at minimizing the influence of such kinetic effects on the sedimentation results.

At low RST, sedimentation results were strongly correlated with the dielectric constants of the solvents (Table A.1). Quickly, a discrimination however appears among highly dielectric solvents and, at a RST of 5.9 $10^{10}$ $s^2m^{-2}$, we were already able to hint "good" solvents from "poor" ones independently of their dielectric constant. At RST = 1.18 $10^{11}$ $s^2m^{-2}$, results are no

longer correlated with the dielectric constants. Highly dielectric solvents like methanol ($\varepsilon_{solv}$=33.0), ethylene glycol (41.4), DMF (38.3), or propylene carbonate (66.1) received the grade 0, while DMSO (47.2) or ethanolamine (31.9) are at 2. The state of sedimentation at RST = 1.18 $10^{11}$ $s^2m^{-2}$ was found to be meta-stable as increasing the RST beyond 1.18 $10^{11}$ $s^2m^{-2}$ no longer affects the results. Vials were kept for months and in volatile media such as chloroform and dichloromethane, the solvent was fully evaporated before any significant change in the suspension turbidity could be observed. It does not mean that the electrostatic stabilizing effect is no longer felt at RST = 1.18 $10^{11}$ $s^2m^{-2}$, but that electrostatic stabilization alone is no longer sufficient to prevent sedimentation at this point. For particles to remain in suspension at high RST, and whatever the level of electrostatic stabilization, there has to be a certain level of chemical affinity. It is this chemical affinity that the HSP analysis seeks to capture.

### *2.3. Thermodynamic approach - Hansen solubility parameters*

#### *2.3.1. Background*

Initially developed to address the issue of the dispersibility of the various components of paints, solubility -or cohesion- parameters theory aims at quantifying the cohesive energy density (taken equal to $\delta_T^2$, MPa) between a chemical and its neighboring media (Hildebrand & Scott, 1950, 1962; Hansen, 2007). Hansen proposed to split the total cohesion parameter, $\delta_T$, into its three main components resulting from the London dispersion forces ($\delta_D$), the dipole-dipole interactions ($\delta_P$), and hydrogen bonding interactions ($\delta_H$) (Hansen 1967a,b, 2007; Hansen & Skaarup, 1967). The linearity of the decomposition in terms of energies means that $\delta_T$ square may then be written as the sum of the squared HSP (Eq. 2). In the HSP theory, every chemical may be represented by a triplet ($\delta_D$, $\delta_P$, $\delta_H$), and then be plotted in a 3 dimensional graph (Hansen, 2007). HSP values of solvents may be determined directly experimentally or estimated by group contribution methods and are now tabulated, alongside those of many commodity polymers (Hansen, 1967b, 2007; Abbott et al., 2018). Gardebjer et al. (2016) used one of these group contribution methods to estimate the HSP of cellulose's repeating unit, cellobiose. They computed a value of ($\delta_D$, $\delta_P$, $\delta_H$) = (16.3; 16.2; 20.7) $MPa^{1/2}$ and assumed it to be the HSP values of CNCs (Gardebjer et al., 2016). Although it provided a quick and easy estimate, the method is unsatisfactory as it does not take into account the fact that polymer HSP are almost systematically greater than those of their repeating units, nor the

fact that crystallinity may greatly affect HSP values (Hansen, 2007; Abbott et al., 2018). Unknown HSP may be determined more accurately through an indirect approach. Affinity tests between the material and various solvents are conducted with the idea that, "like seeking like", the stronger are the interactions the shorter is the distance, $R_a$ ($MPa^{1/2}$, Eq. 3), between their respective Hansen solubility parameters (Hansen, 2007). "Good" solvents, where the "goodness" may be assigned quantitatively (e.g. maximum solubility) or qualitatively (e.g. suspension turbidity or swelling behavior), thus describe a sphere of radius $R_0$ ($MPa^{1/2}$), whose center corresponds to the unknown's HSP (Hansen, 2007). The set of solvents may be completed by mixtures (Machui et al., 2012), Their HSP ($\delta_{D,mix}$ ; $\delta_{P,mix}$ ; $\delta_{H,mix}$) were calculated through Eq. 4 (Hansen, 2007), in which ($\delta_{D,i}$; $\delta_{P,i}$; $\delta_{H,i}$) are the HSP values of the constituent $i$ and $\Phi_i$ its volume fraction; $n$ is the total number of solvents in the mixture.

$$\delta_T^2 = \delta_D^2 + \delta_P^2 + \delta_H^2 \tag{2}$$

$$R_a^2 = 4(\delta_{D,1} \quad \delta_{D,2})^2 + (\delta_{P,1} \quad \delta_{P,2})^2 + (\delta_{H,1} \quad \delta_{H,2})^2 \tag{3}$$

$$\delta_{D,mix} = \sum_{i=1}^{n} \Phi_i \delta_{D,i} \; ; \; \delta_{P,mix} = \sum_{i=1}^{n} \Phi_i \delta_{P,i} \; ; \; \delta_{H,mix} = \sum_{i=1}^{n} \Phi_i \delta_{H,i} \tag{4}$$

Our set of solvents was selected based on their position in the HSP graph to maximize the coverage and based on the uncertainty of the solvents' HSP coordinates. Indeed, the indirect method of HSP determination for an unknown compound is no more precise than that of the solvents that are employed to perform the characterization. Historically, HSP coordinates were determined experimentally for a set of 90 common solvents, from which group contribution models have been derived (Hansen, 2007). Nowadays, and based on these group contribution methods, HSP of thousands of solvents have been calculated (Hansen, 2007; Abbott et al., 2018). When we selected our 27 pure solvents, we aimed at picking them from the list of the 90 experimentally confirmed solvents. Exceptions to the list are ethyl benzoate, heptane, d-limonene, triethanolamine, and water. Water, with its three sets of HSP, is a special case (see Hansen 2007). Heptane, being purely dispersive, has a low uncertainty (uncertainty arises mostly from the calculation of the polar and hydrogen-bonding components: $\delta_P$ and $\delta_H$, respectively) (Abbott et al., 2018). Ethyl benzoate, d-limonene, and triethanolamine HSP values have

been calculated, rather than empirically determined, inducing a greater uncertainty. They were nonetheless selected for their interesting position in the HSP graph.

*2.3.2. HSP analysis*

HSP analysis was performed with the software HSPiP (Abbott et al., 2018). HSP values of pure solvents, binary mixtures, and polymers, were extracted from the HSPiP database (Abbott et al., 2018) and are respectively provided in Tables A.1, A.2, and A.3.

For the sphere fitting, we considered both grade 1 and grade 2-solvents (and mixtures) to be "good" and grade 0-ones to be "poor". The algorithm of the software maximizes the function FIT described below (Eq. 6) (Hansen, 2007; Abbott et al., 2018). The ideal result is a sphere of center ($\delta_{D,s}$ ; $\delta_{P,s}$ ; $\delta_{H,s}$) and of radius $R_0$ that contains all the "good" solvents and mixtures while excluding any "poor" ones. A solvent/mixture is located in the sphere if its distance to the sphere's center, $R_a$ (Eq. 2), is smaller than or equal to $R_0$. It corresponds to a reduced energy difference RED $\leq$ 1 (Eq. 5).

$$RED = R_a/R_0 \tag{5}$$

The quality of the fitting may be assessed through the FIT value and through the uncertainty on the ($\delta_{D,s}$ ; $\delta_{P,s}$ ; $\delta_{H,s}$) coordinates (Hansen, 2007; Abbott et al., 2018). FIT (Eq. 6) is a desirability function (Hansen, 2007) that provides information about the quality of the fit on the $m$ solvents tested : indeed, a "poor" solvent/mixture located inside a sphere (RED $\geq$ 1) or a "good" one located outside (RED $>$ 1) induces a penalty on the FIT coefficient. The better the fit, the closest FIT will be from 1.0 (FIT $\leq$ 1.0). The uncertainty "  ($\Delta\delta_{D,s}$; $\Delta\delta_{P,s}$; $\Delta\delta_{H,s}$)" provides information on the tightness of the HSP sphere core's position. Values in the range of  0.25-0.50 $MPa^{1/2}$ are indicative of a very good fit and of a tight core, while a poor fit will result in uncertainties in the range of  1 $MPa^{1/2}$ (Abbott et al., 2018). It is possible to have a tight core for two parameters and a loose one for the last, meaning that there is a lack of data points in that direction (Abbott et al., 2018). It has to be noted that fitting a sphere on less than 4-5 good solvents necessarily leads to an uncertainty that may not be reflected in the FIT value nor in the "  ($\Delta\delta_{D,s}$; $\Delta\delta_{P,s}$; $\Delta\delta_{H,s}$)". The existence of an uncertainty means that results obtained in running several times the algorithm on the same data differ slightly. Results reported here are those corresponding to

the highest FIT value and the lowest uncertainty over at least 10 runs of the fitting algorithm. The values were overall very stable between the different fits with variations in the range of 0.001 for FIT and of 0.05 $MPa^{1/2}$ for the different uncertainties: $(\Delta\delta_{D,s}; \Delta\delta_{P,s}; \Delta\delta_{H,s})$.

$$FIT = \left[\sum_{i=1}^{m} A_i^m\right]^{1/m}$$

$$\begin{aligned} &\text{For ``good'' solvents inside a sphere}: A_i = 1 \\ &\text{For ``poor'' solvents outside a sphere}: A_i = 1 \\ &\text{For ``good'' solvents outside a sphere}: A_i = e^{+(R_0 - R_a)} \\ &\text{For ``poor'' solvents inside a sphere}: A_i = e^{+(R_a - R_0)} \end{aligned} \quad (6)$$

## 3. Results and discussion

Considering both grade 2 and 1 as "good" solvents, two distinct regions of preferential dispersibility may clearly be distinguished. The first is in the polar region of the graph (high $\delta_P$ and $\delta_H$, Fig. 2.c) and contains all of the grade 2 solvents: dimethylsulfoxide (DMSO), formamide, water, and ethanolamine. The area delimited by these solvents is bordered by 0-grade ones like triethanolamine, propylene carbonate, N,N-dimethylformamide, or acetone. A second distinct region may then be distinguished in the mildly non-polar region (intermediate $\delta_P$ and $\delta_H$) where chloroform and dichloromethane are classified as grade 1 and stand alone surrounded by poor solvents. This behavior, with two distinct regions, is expected in the HSP theory for amphiphilic species such as particles or block copolymers for instances (Hansen, 2007). In this configuration, two HSP spheres, which correspond to the different affinities of the chemical, may be drawn.

For a better HSP fit, sedimentation tests were performed for binary mixtures of DMSO + acetone, toluene, and methanol, and binary mixtures of formamide + methanol and 1-propanol. Results obtained with binary mixtures validate our scale of dispersibility as the "goodness" of a grade 2 solvent like DMSO decreases to grade 1 once 40 vol% of methanol, a grade 0 solvent, is added and then to 0 beyond 60 vol% (Fig. A.2.b&e). DMSO is known to be one of the best solvent for CNCs dispersion as it enables strong gel formation upon heating (Sojoudiasli et al., 2017).

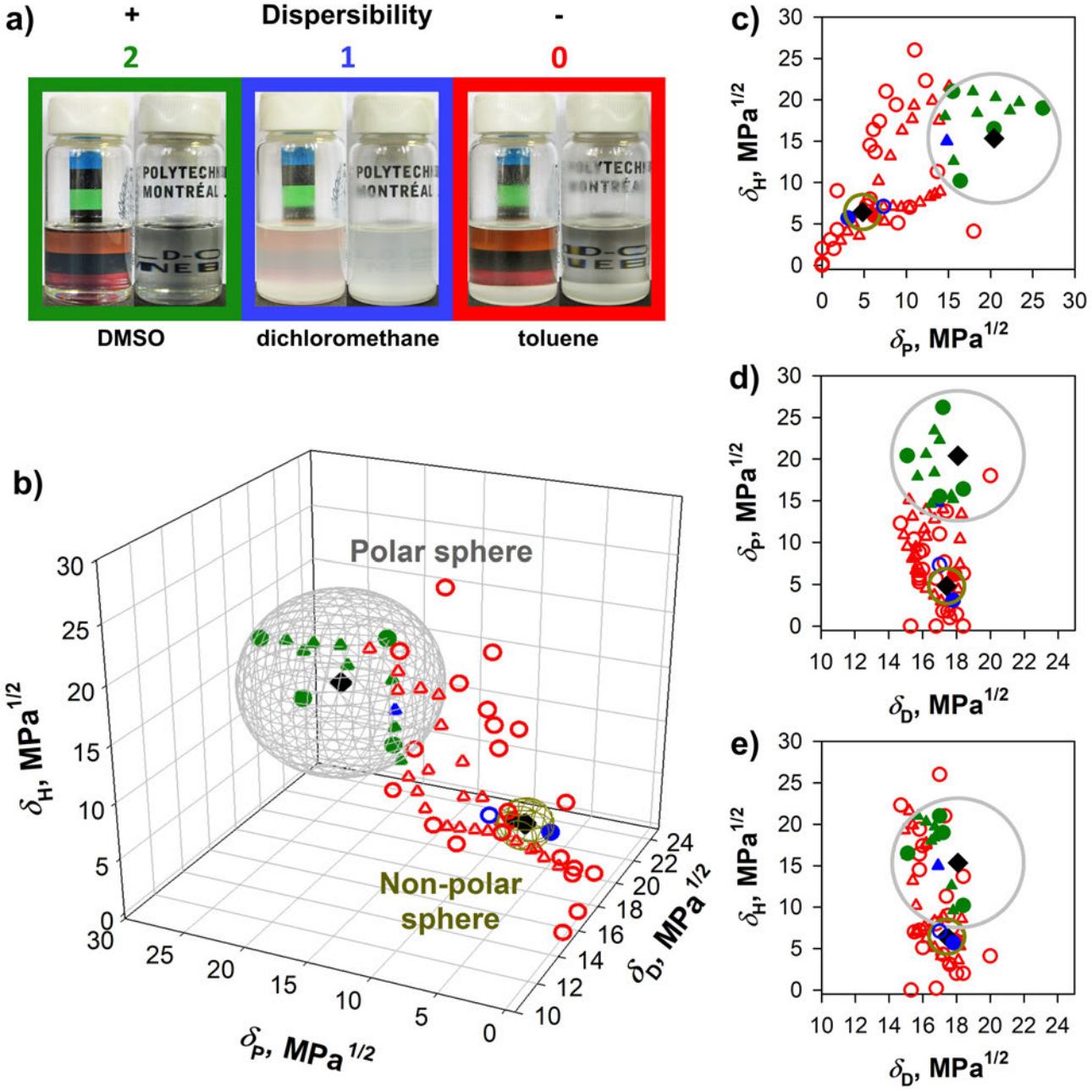


Figure 2: HSP graph of wood-based sulfuric acid-hydrolyzed CNCs.(a) CNC scale of dispersibility. Three di erent grades were attributed to the CNC state of dispersion, from best to worst: 2-in green-No sediment at the bottom of the vial, 1-in blue-Presence of a sediment, the suspension is too turbid to be able to read a text through, 0-in red-Presence of a sediment, the suspension is less turbid/clear. Pure solvents are represented by circles, binary mixtures by triangles, sphere centers by black diamonds. Two di erent spheres may be plotted : a large polar sphere ($\delta_D$; $\delta_P$; $\delta_H$) = (18.1; 20.4; 15.3) (0.5; 0.5; 0.4) $MPa^{1/2}$ and another smaller sphere in the mildly non-polar region ($\delta_D$; $\delta_P$; $\delta_H$) = (17.4; 4.8; 6.5) (0.3; 0.5; 0.6) $MPa^{1/2}$. Symbols located inside a sphere are full and symbols outside are empty. The HSP graph is represented in a 3-dimensional view (b), and in 2-dimensional views alongside the planes $\delta_H$-$\delta_P$ (c), $\delta_P$-$\delta_D$ (d), and $\delta_H$-$\delta_D$ (e).

Using HSPiP (Hansen Solubility Parameters in Practice) software (Abbott et al., 2018), it was possible to obtain a well defined sphere ($\mathsf{FIT}$ = 1.0, see Eq. 6) of radius $R_{0,P}$=7.8 $MPa^{1/2}$ in the polar region. It includes 13 good solvents and mixtures while excluding any poor ones. Its center's coordinates ($\delta_D$; $\delta_P$; $\delta_H$) are (18.1; 20.4; 15.3) (0.5; 0.5; 0.4) $MPa^{1/2}$ for a $\delta_T$ of 31.3 1.6 $MPa^{1/2}$. Having defined with precision what stands clearly for the dominant affinity of CNCs, the case of chloroform and dichloromethane may be addressed. These results are concordant with reports by Yu et al. of stable suspensions of sulfuric acid hydrolyzed CNCs in chloroform (Yu & Qin, 2012; Yu et al., 2012). A fitting in this area of the graph yields a $\mathsf{FIT}$ of 0.974 with a sphere of radius $R_{0,P}$=2.1 $MPa^{1/2}$ and centered about ($\delta_D$; $\delta_P$; $\delta_H$) = (17.4; 4.8; 6.5) (0.3; 0.5; 0.6) $MPa^{1/2}$. It corresponds to a $\delta_T$ of 19.2 2.7 $MPa^{1/2}$. Here, the $\mathsf{FIT}$ value is lowered by ethyl benzoate, which is a 0-grade solvent despite having HSP close to that of dichloromethane and chloroform. It is not clear whether it highlights a limitation of the HSP method itself –as we know that conformation effects for instance are not accounted for in HSP theory– or a limitation of the HSP group contribution models. Ethyl benzoate is indeed among the few solvents we employed whose HSP were calculated without any experimental confirmation (Hansen, 2007). It may thus be that the $\mathsf{FIT}$ value is only lowered by imprecise solvent coordinates: ethyl benzoate while being plotted as inside of the non-polar sphere (Fig. 2) may actually be out of it. From the 90 solvents experimentally proofed by Hansen and co-workers (1967; 1967a; 1967b), and aside from chloroform and dichloromethane, none is located in the area of interest. This issue cannot be settled easily with the current experimental method. Fitted using only two good solvents, the position of the non-polar sphere thus has to be considered with caution. It however provides the first experimental estimates of CNC hydrophobic surface HSP.

The polar sphere is considered to correspond to the HSP of the hydroxyl rich (110) and $(1\bar{1}0)$ surfaces. Computer simulations indeed predicts that (110) and $(1\bar{1}0)$ surfaces have similar surface energies (Yamane et al., 2006) and hydrophilicity (Heiner et al., 1998; Matthews et al., 2006), which means that they are expected to be represented by a single HSP sphere (Table 1). Meanwhile, the mildly non-polar sphere is attributed to the display of (200) surfaces by the nanocrystals. Their lower simulated surface energy (Yamane et al., 2006) and higher modeled water contact angle (Mazeau & Rivet, 2008) are indeed expected to result into a distinct HSP sphere.

The contrast between the better fit and wider radius of the polar sphere

and the lesser ones of the non-polar sphere is coherent with the fact that sulfuric acid hydrolyzed CNCs have been reported to exhibit experimentally a predominant polar and hydrophilic behavior. HSP of the polar sphere are furthermore very close to those obtained for the chemical accessibility of cellulose : $(\delta_D;\ \delta_P;\ \delta_H) = (19.09;\ 15.77;\ 15.29) \quad (0.15;\ 0.25;\ 0.30)\ \mathrm{MPa}^{1/2}$ (Hansen & Björkman, 1998; Larsson & Johns, 1988; Minhas & Robertson, 1967). These are calculated from the ability of different solvents to swell cotton-based $I_\alpha$ cellulose pulp. Swelling increases the active surface area of the pulp by increasing hydroxyl group accessibility, the amount of which is quantified chemically through a thallation of the -OH functions (Minhas & Robertson, 1967). The only significant deviation lies in $\delta_P$, the polar component, that is increased by $+4.6\,\mathrm{MPa}^{1/2}$ from the chemical accessibility of cellulose HSP to our polar sphere's results. Slight variations in $\delta_D$ and $\delta_H$, coupled to a sharp increase in $\delta_P$ are coherent with the effect of surface sulfatation based on the predictions of HSP group contributions (Stefanis & Panayiotou, 2008). The $\delta_P$ increase for CNCs with respect to the cotton-based pulp is thus attributed to the introduction of sulfate groups on the hydroxyl groups of the nanocrystal surfaces during the sulfuric acid hydrolysis (Hamad & Hu, 2010; Hamad, 2017). Part of this variation is also probably imputable to the difference in wettability between $I_\alpha$ and $I_\beta$ hydroxyl-rich surfaces, although simulations predict very similar surface energies with $154\,\mathrm{mN\,m^{=1}}$ and $155\,\mathrm{mN\,m^{=1}}$, respectively (Yamane et al., 2006).

It is worth noting that this shift of $+4.6\,\mathrm{MPa}^{1/2}$ in $\delta_P$ reduces the HSP distance of CNCs with water from $9.3\,\mathrm{MPa}^{1/2}$ to $6.1\,\mathrm{MPa}^{1/2}$, which may be able to partly explain the increased affinity of sulfated CNCs for water. As contact angles have usually been found experimentally to be positively correlated with HSP distance (Hansen, 2007), this finding is also coherent with the water contact angle value obtained by simulation by Mazeau & Rivet (2008). The 43° of the (110) surface corresponds to a HSP distance of $6.1\,\mathrm{MPa}^{1/2}$, while the 95° of the (200) surface corresponds, based on our results, to a HSP distance of $19.1\,\mathrm{MPa}^{1/2}$.

From our knowledge of the CNC structure, it is thus possible to assign each of the spheres to a lattice plane, which enables us for the first time to estimate the amphiphilicity of wood-based sulfated CNCs. Our results also highlight the limitations of group contribution methods to estimate cellulose nanocrystal HSP. Given that they do not take into account conformation effects, computations by Gardebjer et al. (2016) were not able to predict a second non-polar sphere for CNCs. If we compare their results to those

of our polar sphere, they also underestimate $\delta_D$ and $\delta_P$ by 1.7 $MPa^{1/2}$ and 4.2 $MPa^{1/2}$, respectively, which is not unexpected when HSP of a polymer are compared to those of its repeating unit (Hansen, 2007). The hydrogen bonding component, $\delta_H$, was underestimated by 5.4 $MPa^{1/2}$ (Gardebjer et al., 2016). It may probably be attributed to the fact that the influence of the -OH groups of cellulose is hindered by their involvement in the crystalline network of CNCs (Jarvis, 2003; Djahedi et al., 2016).

The amphiphilicity of cellulose chains has recently been advanced as a key-factor to explain the low solubility of cellulose chains in polar solvents (Medronho et al., 2012). This parameter was not considered by Hansen & Björkman (1998) when they worked on wood ultrastructure and cellulose affinity. While Fig. 2 provides experimental evidence for this amphiphilicity, we believe that due to the high dependency of HSP with conformation effects, such as those induced by crystallinity (Hansen, 2007; Abbott et al., 2018), any extrapolation from crystalline to amorphous cellulose has to be considered with great caution. Our interest in HSP instead lies in their ability to represent in a same graph –thus enabling comparisons– chemicals of very different scales, from solvents to polymers, (nano)particles, and macroscale surfaces. Determining HSP of cellulose nanocrystals, based on their behavior in a set of solvents, may thus provide information about their affinity for polymer matrices. HSP of some common polymer matrices, such as poly(vinyl alcohol) (PVOH), poly(lactic acid) (PLA), poly(ethylene glycol) (PEG), poly(methyl methacrylate) (PMMA), poly(ethylene) (PE), and poly(propylene) (PP), are available (Abbott et al., 2018) and are plotted in the Fig. 3. It is worth pointing out that the HSP values of polymers are notably functions of their molecular weight and degree of crystallinity (Hansen, 2007; Abbott et al., 2018) and the parameters employed here are average values as provided in the HSPiP polymer dataset (Abbott et al., 2018). These polymers may be split into 3 groups based on their HSP: I-in the polar sphere (PVOH), II-in between the spheres (PEG, PLA, PMMA) and III-in the non-polar region (PE and PP). CNC-polymer affinity is not the only factor at play for CNC dispersion in polymer matrices.

The protocol employed (melt mixing or solvent casting) has, for instance, a major influence (Bagheriasl et al., 2016, 2017). Assuming that the quality of CNC dispersion in the solvent is important for solvent casting, then other parameters such as the "goodness" of the solvent (Fig. 2), the initial state of CNCs (Beuguel et al., 2018b; Peng et al., 2016) –the use of never-dried, freeze-dried, or spray-dried–, and the protocol employed for the dispersion –such as

ultrasonication conditions (Beuguel et al., 2018a)– are also relevant. Keeping these points in mind, it is striking how these polymer-categories (I, II, and III), based solely on HSP, match with the experimental quality reported for the dispersion of sulfuric acid-hydrolyzed CNCs in the aforementioned matrices: PVOH has been reported to be one of the best matrices for CNC dispersion both in solvent casting and melt mixing (Hamad, 2017), which is coherent with it being in the dominant polar sphere of CNCs. A good dispersion of CNCs is also achievable in PLA (Zhang et al., 2015; Bagheriasl et al., 2016, 2017), PEG (Beuguel et al., 2018a; Yao et al., 2017; Zhou et al., 2011; Xu et al., 2013, 2014), and PMMA (Yin et al., 2016) through a solvent casting. Direct melt mixing may however remain difficult for this group II-polymers as in the case of PLA (Raquez et al., 2013; Khoshkava & Kamal, 2013; Dhar et al., 2016; Bagheriasl et al., 2017).

Dhar et al. (2016) demonstrated that the sulfatation of CNC surfaces lessens their dispersibility in PLA matrices, which is consistent with our HSP results: the shift of $+4.6\,\mathrm{MPa}^{1/2}$ in the $\delta_P$ of the polar sphere between sulfated CNCs and chemically accessible cellulose increases the distance between the PLA matrices and the (110) and $(1\bar{1}0)$ surfaces' sphere from $11.4$ to $15.0\,\mathrm{MPa}^{1/2}$. Based on the HSP theory, the absence of any adsorption of PEG on CNC surfaces (Beuguel et al., 2018a; Reid et al., 2017) is also coherent with this polymer being out of any sphere, adsorption being only expected for compounds of very similar HSP (Hansen, 1997). Modification of the nanocrystal OH groups, which is expected to result in a shift of the corresponding surfaces HSP sphere (Peng et al., 2016; Yoo & Youngblood, 2016), may significantly improve the CNC dispersion and the reinforcing effect in group II-matrices (Raquez et al., 2013; Yin et al., 2016; Zhang et al., 2015; Khoshkava & Kamal, 2013). It is likely that a systematic HSP characterization of the modified CNCs would have concluded that any chemical modification that improves the CNC dispersion in a matrice also reduces the HSP distance between the polar sphere and this matrix, as in the case of Peng et al. (2017). In group III-matrices such as PP (Bagheriasl et al., 2015; Khoshkava & Kamal, 2014) and PE (Lewandowska & Eichhorn, 2016; Inai et al., 2018), nanoscale dispersion in melt compounding seems to be impossible without the use of a compatibilizer. While unmodified nanocrystals have an interfacial tension with PP more than fourfold that with PLA, surface modification may, here again, shift the relative affinity of CNCs and make dispersion more favorable in PP with a slightly lower interfacial tension (Khoshkava & Kamal, 2014). Probably due to the low solubility of

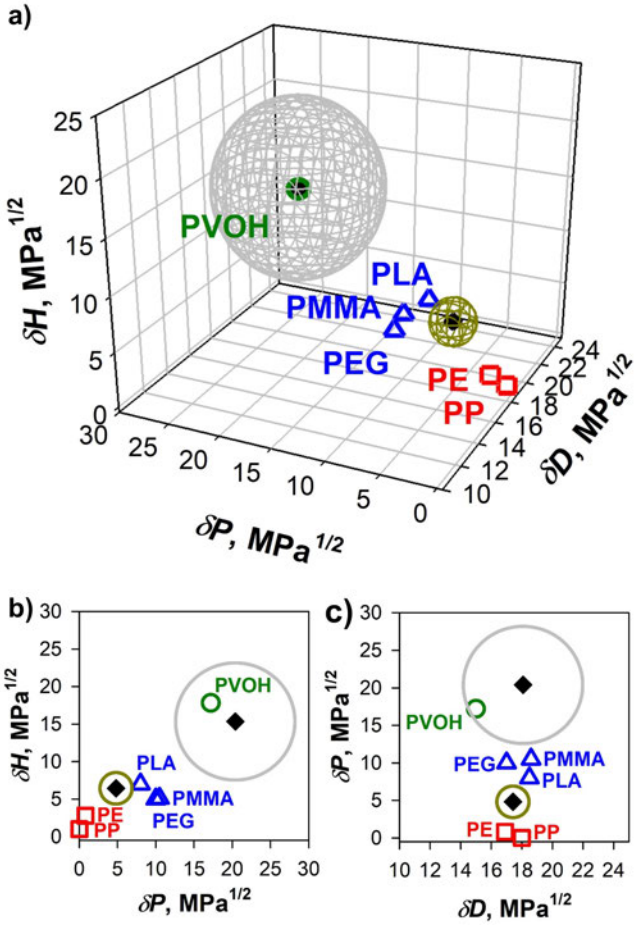


Figure 3: HSP graph of wood-based sulfuric acid hydrolyzed CNCs (see Fig. 2) compared to some commodity polymers. These polymers may be split into 3 groups based on their HSP (Abbott et al., 2018): I-green circles-in the polar sphere for poly(vinyl alcohol) (PVOH); II-blue triangles-in between the spheres for poly(lactic acid) (PLA), poly(ethylene glycol) (PEG), and poly(methyl methacrylate) (PMMA); and III-red squares-in the non-polar region for poly(ethylene) (PE), and poly(propylene) (PP). Categories I, II, and III match, from best to worst, with experimental reports for the dispersibility of CNCs in these matrices. The HSP graph is represented in a 3-dimensional view **(a)**, and in 2-dimensional views alongside the planes $\delta_H$-$\delta_P$ **(b)**, and $\delta_P$-$\delta_D$ **(c)**.

these polymers in common solvents (Hansen, 2007), no experimental data are available for the solvent casting of these PP and PE nanocomposites.

## 4. Concluding remarks

In conclusion, we linked CNC dispersibility in a large set of solvents and binary mixtures to the anisotropy of the nanocrystal structure. Wood-based sulfuric acid-hydrolyzed CNCs were found to be predominantly polar particles with a main HSP sphere of radius 7.8 $MPa^{1/2}$ and of center ($\delta_D$ ; $\delta_P$ ; $\delta_H$) = (18.1; 20.4; 15.3) (0.5; 0.5; 0.4) $MPa^{1/2}$. This main behavior is thought to reflect the influence of their hydroxyl-rich (110) and ($1\bar{1}0$) surfaces and is coherent with their behavior described in the literature. While predicted years ago through simulations and expected based on cross-sectional structure analysis of the nanocrystals through X-ray scattering and AFM techniques, this study is the first to experimentally confirm the contribution of hydrophobic surfaces to the behavior of CNCs in suspensions. We provide an approximation of their chemical influence through the determination of their Hansen solubility parameters (HSP). Although refinements are still necessary, as based only on two good solvents, the non-polar sphere location is estimated in the range of (17.4; 4.8; 6.5) (0.3; 0.5; 0.6) $MPa^{1/2}$ with a radius of 2.1 $MPa^{1/2}$. This position, relatively to that of the polar sphere, is coherent with results from computer simulations for the display of (200) lattice planes by the CNC particles. Further work is required to determine the influence of the feedstock, of the hydrolysis conditions, and of the dispersion protocol on the display of an amphiphilic behavior by CNCs.

HSP graphs are a useful tool to predict the CNC dispersion in polymer matrices and allow us a better understanding of results already published in the literature. Such characterization could be carried out on functionalized particles to understand the effect of the chemical modification on the surface properties of the nanocrystals (Yoo & Youngblood, 2016; Peng et al., 2016) and on their dipersibility (Peng et al., 2017) in non-polar media.

## Conflicts of interest

There are no conflicts to declare

## Acknowledgments

The authors acknowledge the financial contributions of FPInnovations (Pointe-Claire, QC, Canada), of PRIMA Québec (grant number FPI NCC RD001), of the National Science and Engineering Research Council (NSERC,

grant number RDCPJ 490786-15). The Fond de Recherche du Québec - Nature et Technologies (FRQNT) kindly provided C. Bruel with a scholarship (number 208324). Celluforce (Montréal, QC, Canada) is also gratefully acknowledged for providing the cellulose nanocrystals. The authors would like to thank Dr. W. Y. Hamad, from FPInnovations, for his contribution in reviewing this work. We are grateful to Dr. Q. Beuguel for his contribution to the TEM and EDX analyses. Finally, Mr. J.-P. Masse is acknowledged for his help with the XRD analysis.

## References

Abbott, S. J., Hansen, C. M., & Yamamoto, H. (2018). Hansen solubility parameters in practice software, ebook, datasets. Url: http://www.hansen-solubility.com, accessed on 2018/07/03.

Atalla, R. H., & Vanderhart, D. L. (1999). The role of solid state 13C NMR spectroscopy in studies of the nature of native celluloses. *Solid State Nucl. Magn. Reson.*, *15*, 1–19.

Bagheriasl, D., Carreau, P. J., Dubois, C., & Riedl, B. (2015). Properties of polypropylene and polypropylene/poly(ethylene-co-vinyl alcohol) blend/CNC nanocomposites. *Compos. Sci. Technol.*, *117*, 357–363.

Bagheriasl, D., Carreau, P. J., Riedl, B., Dubois, C., & Hamad, W. Y. (2016). Shear rheology of polylactide (PLA)âĂŞcellulose nanocrystal (CNC) nanocomposites. *Cellulose*, *23*, 1885–1897.

Bagheriasl, D., Safdari, F., Carreau, P. J., Dubois, C., & Riedl, B. (2017). Development of cellulose nanocrystal-reinforced polylactide: A comparative study on different preparation methods. *Polym. Cpmpos.*, . DOI: 10.1002/pc.24676.

Beuguel, Q., Tavares, J. R., Carreau, P. J., & Heuzey, M.-C. (2018a). Rheological behavior of cellulose nanocrystal suspensions in polyethylene glycol. *J. Rheol.*, *62*, 607–618.

Beuguel, Q., Tavares, J. R., Carreau, P. J., & Heuzey, M.-C. (2018b). Ultrasonication of spray- and freeze-dried cellulose nanocrystals in water. *J. Colloid Interface Sci.*, *516*, 23–33.

Brown, R. M. (1996). The biosynthesis of cellulose. J. Macromol. Sci., Part A: Pure Appl. Chem., A33, 1345–1373.

Chaturvedi, K., Ganguly, K., Kulkarni, A. R., Kulkarni, V. H., Nadagouda, M. N., Rudzinski, W. E., & Aminabhavi, T. M. (2011). Cyclodextrin-based siRNA delivery nanocarriers: a state-of-the-art review. Expert Opin. Drug Del., 8, 1455–1468.

Conley, K. M., Godbout, L., Whitehead, M. A., & van de Ven, T. G. M. (2017a). Reversing the structural chirality of cellulosic nanomaterials. Cellulose, 24, 5455–5462.

Conley, K. M., Whitehead, M. A., & van de Ven, T. G. M. (2017b). Probing the structural chirality of crystalline cellulose with induced circular dichroism. Cellulose, 24, 479–486.

Cousins, S. K., & Brown, R. M. (1995). Cellulose I microfibril assembly: computational molecular mechanics energy analysis favours bonding by van der Waals forces as the initial step in crystallization. Polymer, 36, 3885–3888.

Dhar, P., Bhasney, S. M., Kumar, A., & Katiyar, V. (2016). Acid functionalized cellulose nanocrystals and its effect on mechanical, thermal, crystallization and surfaces properties of poly (lactic acid) bionanocomposites films: A comprehensive study. Polymer, 101, 75–92.

Ding, S.-Y., & Himmel, M. E. (2006). The Maize Primary Cell Wall Microfibril: A New Model Derived from Direct Visualization. J. Agric. Food Chem., 54, 597–606.

Ding, S.-Y., Liu, Y.-S., Zeng, Y., Himmel, M. E., Baker, J. O., & Bayer, E. A. (2012). How Does Plant Cell Wall Nanoscale Architecture Correlate with Enzymatic Digestibility? Science, 338, 1055–1060.

Ding, S.-Y., Zhao, S., & Zeng, Y. (2014). Size, shape, and arrangement of native cellulose fibrils in maize cell walls. Cellulose, 21, 863–871.

Djahedi, C., hle Wohlert, M. B., Berglund, L. A., & Wohlert, J. (2016). Role of hydrogen bonding in cellulose deformation-the leverage effect analyzed by molecular modeling. Cellulose, 23, 2315–2323.

Dufresne, A. (2017). *Nanocellulose. From Nature to High Performance Tailored Materials*. (2nd ed.). Berlin/Boston: Walter de Gruyter GmbH.

Elazzouzi-Hafraoui, S., Nishiyama, Y., Putaux, J.-L., Heux, L., Dubreuil, F., & Rochas, C. (2008). The shape and size distribution of crystalline nanoparticles prepared by acid hydrolysis of native cellulose. *Biomacromolecules*, *9*, 57–65.

Eyley, S., & Thielemans, W. (2014). Surface modification of cellulose nanocrystals. *Nanoscale*, *6*, 7764–7779.

French, A. D. (2017). Glucose, not cellobiose, is the repeating unit of cellulose and why that is important. *Cellulose*, *24*, 4605–4609.

Gardebjer, S., Andersson, M., Engström, J., Restorp, P., Persson, M., & Larsson, A. (2016). Using Hansen solubility parameters to predict the dispersion of nano-particles in polymeric films. *Polym. Chem.*, *7*, 1756–1764.

Habibi, Y., Lucia, L. A., & Rojas, O. J. (2010). Cellulose Nanocrystals: Chemistry, Self-Assembly, and Applications. *Chem. Rev.*, *110*, 3479–3500.

Hamad, W. Y. (2017). *Cellulose Nanocrystals Properties, Production and Applications*. Chichester, U. K.: Wiley.

Hamad, W. Y., & Hu, T. Q. (2010). Structure-process-yield interrelation in nanocrystalline cellulose extraction. *Can. J. Chem. Eng.*, *88*, 392–402.

Hansen, C. M. (1967a). The Three Dimensional Solubility Parameter - Key to Paint Component Affinities I. - Solvents, Plasticizers, Polymers, and Resins. *J. Paint Techn.*, *39*, 104–117.

Hansen, C. M. (1967b). *The Three Dimensional Solubility Parameter and Solvent Diffusion Coefficient, Their Importance in Surface Coating Formulation*. Ph.D. thesis Technical University of Denmark Copenhagen, Danemark.

Hansen, C. M. (1997). Cohesion Parameters for Surfaces, Pigments, and Fillers. *Surf. Coat. Int.*, *8*, 386–391.

Hansen, C. M. (2007). *Hansen Solubility Parameters A User's Handbook*. Boca Raton, FL, U. S. A.: CRC Press.

*Holzforschung 52*

*J. Paint Techn. 39*

*Carbohyd. Res. 306*

*The Solubility of Nonelectrolytes*

*Regular Solutions*

*Science 315*

*Compos. Sci. Technol. 154*

*Nature 426*

*Biomacromolecules 14*

*Powder Technol. 261*

*Surface Chemistry of Surfactants and Polymers*

*J. Microsc.-Oxford 178*

Larsson, A., & Johns, W. E. (1988). Acid-base interactions between cellulose/lignocellulose and organic molecules. *J. Adhesion*, *25*, 121–131.

Lewandowska, A. E., & Eichhorn, S. J. (2016). Raman imaging as a tool for assessing the degree of mixing and the interface between polyethylene and cellulose nanocrystals. *IOP Conf. Ser. Mater. Sci. Eng.*, *139*, 012030.

Li, Q., & Renneckar, S. (2011). Supramolecular Structure Characterization of Molecularly Thin Cellulose I Nanoparticles. *Biomacromolecules*, *12*, 650–659.

Liu, D., Chen, X., Y.Yue, Chen, M., & Wu, Q. (2011). Structure and rheology of nanocrystalline cellulose. *Carbohydr. Polym.*, *84*, 311–322.

Machui, F., Langner, S., Zhu, X., Abbott, S., & Brabec, C. J. (2012). *Sol. Energ. Mat. Sol. C.*, *100*, 138–146.

Marques, H. M. C. (2010). A review on cyclodextrin encapsulation of essential oils and volatiles. *Flavour Frag. J.*, *25*, 313–326.

Matthews, J. F., Skopec, C. E., Mason, P. E., Zuccato, P., Torget, R. W., Sugiyama, J., Himmel, H. E., & Brady, J. W. (2006). Computer simulation studies of microcrystalline cellulose Iβ. *Carbohyd. Res.*, *341*, 138–152.

Mazeau, K., & Rivet, A. (2008). Wetting the (110) and (100) Surfaces of Iβ Cellulose Studied by Molecular Dynamics. *Biomacromolecules*, *9*, 1352–1354.

Mazeau, K., & Wyszomirski, M. (2012). Modelling of Congo red adsorption on the hydrophobic surface of cellulose using molecular dynamics. *Cellulose*, *19*, 1495–1506.

Medronho, B., Romano, A., Miguel, M. G., Stigsson, L., & Lindman, B. (2012). Rationalizing cellulose (in)solubility: reviewing basic physicochemical aspects and role of hydrophobic interactions. *Cellulose*, *19*, 581–587.

Minhas, P. S., & Robertson, A. A. (1967). Accessibility of Cellulose by the Thallous Ethylate Method-Application to the Measurement of Cellulose Liquid Interactions 1. *Textile Res. J.*, *37*, 400–408.

642 Moon, R. J., Martini, A., Nairn, J., Simonsen, J., & Youngblood, J. (2011).
643 Cellulose nanomaterials review: structure, properties and nanocomposites.
644 Chem. Soc. Rev., 40, 3941–3994.

645 Nishiyama, Y. (2017). Molecular interactions in nanocellulose assembly. Phil.
646 Trans. R. Soc. A., 376, 20170047.

647 Nishiyama, Y., Langan, P., & Chanzy, H. (2002). Crystal Structure and
648 Hydrogen-Bonding System in Cellulose $I_\beta$ from Synchrotron X-ray and
649 Neutron Fiber Diffraction. J. Am. Chem. Soc, 124, 9074–9082.

650 Nishiyama, Y., Sugiyama, J., Chanzy, H., & Langan, P. (2003). Crystal
651 Structure and Hydrogen Bonding System in Cellulose $I_\alpha$ from Synchrotron
652 X-ray and Neutron Fiber Diffraction. J. Am. Chem. Soc, 125, 14300–
653 14306.

654 Peng, S. X., Chang, H., Kumar, S., Moon, R. J., & Youngblood, J. P. (2016).
655 A comparative guide to controlled hydrophobization of cellulose nanocrys-
656 tals via surface esterification. Cellulose, 23, 1825–1846.

657 Peng, S. X., Shrestha, S., Yoo, Y., & Youngblood, J. P. (2017). Enhanced
658 dispersion and properties of a two-component epoxy nanocomposite using
659 surface modified cellulose nanocrystals. Polymer, 112, 359–368.

660 Petersson, L., Kvien, I., & Oksman, K. (2007). Structure and thermal proper-
661 ties of poly(lactic acid)/cellulose whiskers nanocomposite materials. Com-
662 pos. Sci. Technol., 67, 2535–2544.

663 Raquez, J.-M., Habibi, Y., Murariu, M., & Dubois, P. (2013). Polylactide
664 (PLA)-based nanocomposites. Prog. Polym. Sci., 38, 1504–1542.

665 Reid, M. S., Villalobos, M., & Cranston, E. D. (2017). The role of hydro-
666 gen bonding in non-ionic polymer adsorption to cellulose nanocrystals and
667 silica colloids. Curr. Opin. Colloid In. , 29, 76–82.

668 Sèbe, G., Ham-Pichavant, F., Ibarboure, E., Koffi, A. L. C., & Tingaut,
669 P. (2012). Supramolecular Structure Characterization of Cellulose II
670 Nanowhiskers Produced by Acid Hydrolysis of Cellulose I Substrates.
671 Biomacromolecules, 13, 570–578.

Segal, L., Creely, J. J., Martin, Jr, A. E., & Conrad, C. M. (1959). An Empirical Method for Estimating the Degree of Crystallinity of Native Cellulose Using the X-Ray Diffractometer. *Text. Res.*, *29*, 786–794.

Siqueira, G., Bras, J., & Dufresne, A. (2010). New Process of Chemical Grafting of Cellulose Nanoparticles with a Long Chain Isocyanate. *Langmuir*, *26*, 402–411.

Sojoudiasli, H., Heuzey, M.-C., Carreau, P. J., & Riedl, B. (2017). Rheological behavior of suspensions of modified and unmodified cellulose nanocrystals in dimethyl sulfoxide. *Rheol. Acta*, *56*, 673–682.

Stefanis, E., & Panayiotou, C. (2008). Prediction of Hansen Solubility Parameters with a New Group-Contribution Method. *Int. J. Thermophys.*, *29*, 568–585.

Uhlig, M., Fall, A., Wellert, S., Lehmann, M., Prévost, S., Wågberg, L., von Klitzing, R., & Nyström, G. (2016). Two-dimensional aggregationand semidilute ordering in cellulose nanocrystals. *Langmuir*, *32*, 442–450.

Usov, I., Nyström, G., Adamcik, J., Handschin, S., Schütz, C., Fall, A., Bergström, L., & Mezzenga, R. (2015). Understanding nanocellulose chirality and structureâĂŞproperties relationship at the single fibril level. *Nat. Commun.*, *6*, 7564.

Wade, R. H., & Creely, J. J. (1974). Structure and Stability of Chloroform-Included Cotton Cellulose1. *Text. Res. J.*, *44*, 941–945.

Xu, X., Liu, F., Jiang, L., Zhu, J. Y., Haagenson, D., & Wiesenborn, D. P. (2013). Cellulose Nanocrystals vs. Cellulose Nanofibrils: A Comparative Study on Their Microstructures and Effects as Polymer Reinforcing Agents. *ACS Appl. Mater. Inter.*, *5*, 2999–3009.

Xu, X., Wang, H., Jiang, L., Wang, X., Payne, S. A., Zhu, J. Y., & Li, R. (2014). Comparison between Cellulose Nanocrystal and Cellulose Nanofibril Reinforced Poly(ethylene oxide) Nanofibers and Their Novel Shish-Kebab-Like Crystalline Structures. *Macromolecules*, *47*, 3409–3416.

Yamane, C., Aoyagi, T., Ago, M., Sato, K., Okajima, K., & Takahashi, T. (2006). Two different surface properties of regenerated cellulose due to structural anisotropy. *Polym. J.*, *38*, 819–826.

Yao, K., Meng, Q., Bulone, V., & Zhou, Q. (2017). Flexible and Responsive Chiral Nematic Cellulose Nanocrystal/Poly(ethylene glycol) Composite Films with Uniform and Tunable Structural Color. *Adv. Mater.*, *29*, 1701323.

Yin, Y., Tian, X., Jiang, X., Wang, H., & Gao, W. (2016). Modi cation of cellulose nanocrystal via SI-ATRP of styrene and the mechanism of its reinforcement of polymethylmethacrylate. *Carbohydr. Polym.*, *142*, 206 212.

Yoo, Y., & Youngblood, J. P. (2016). Green One-Pot Synthesis of Surface Hydrophobized Cellulose Nanocrystals in Aqueous Medium. *ACS Sustainable Chem. Eng.*, *4*, 3927 3938.

Yu, H., & Qin, Z. (2012). E ect of Cellulose nanocrystal on Crystallization Behavior of Poly(3â€“hydroxybutyrateâ€“coâ€“3â€“hydroxyvalerate). *Adv. Mat. Res.*, *430-432*, 20 23.

Yu, H.-Y., Qin, Z.-Y., Liu, Y.-N., Chen, L., Liu, N., & Zhou, Z. (2012). Simultaneous improvement of mechanical properties and thermal stability of bacterial polyester by cellulose nanocrystals. *Carbohydr. Polym.*, *89*, 971 978.

Zhang, C., Salick, M. R., Cordie, T. M., Ellingham, T., Dan, Y., & Turng, L.-S. (2015). Incorporation of poly(ethylene glycol) grafted cellulose nanocrystals in poly(lactic acid) electrospun nanocomposite bers as potential scaffolds for bone tissue engineering. *Mater. Sci. Eng. C Mater. Biol. Appl.*, *49*, 463 471.

Zhou, C., Chu, R., Wu, R., & Wu, Q. (2011). Electrospun polyethylene oxide/cellulose nanocrystal composite nano brous mats with homogeneous and heterogeneous microstructures. *Biomacromolecules*, *12*, 2617 2625.